Chinese Chemical Letters 35 (2024) 109258

Contents lists available at ScienceDirect

Chinese Chemical Letters

journal homepage: www.elsevier.com/locate/cclet

Highly dispersed Ru nanospecies on N-doped carbon/MXene composite for highly efficient alkaline hydrogen evolution

Minying Wu[a], Xueliang Fan[a], Wenbiao Zhang[a], Bin Chen[a], Tong Ye[a], Qian Zhang[a], Yuanyuan Fang[a], Yajun Wang[b,*], Yi Tang[a,*]

[a] Department of Chemistry, Shanghai Key Laboratory of Molecular Catalysis and Innovative Materials, and Laboratory of Advanced Materials, Fudan University, Shanghai 200438, China
[b] College of Chemistry & Materials Engineering, Wenzhou University, Wenzhou 325027, China

ARTICLE INFO

Article history:
Received 21 August 2023
Revised 26 October 2023
Accepted 26 October 2023
Available online 2 November 2023

Keywords:
HER activity
Highly dispersed
Ru-based catalysts
MXene
Alkaline condition

ABSTRACT

Hydrogen has emerged as a promising environmentally friendly energy source. The development of low-cost, highly active, stable, and easily synthesized catalysts for hydrogen evolution reactions (HER) remains a significant challenge. This study explored the synthesis of nitrogen-doped MXene-based composite catalysts for enhanced HER performance. By thermally decomposing $RuCl_3$ coordinated with melamine and formaldehyde resin, we successfully introduced nitrogen-doped carbon (N–C) with highly dispersed ruthenium (Ru) onto the MXene surface. The calcination temperature played a crucial role in controlling the size of Ru nanoparticles (Ru NPs) and the proportion of Ru single-atom (Ru SA), thereby facilitating the synergistic enhancement of HER performance by Ru NPs and Ru SA. The resulting catalyst prepared with a calcination temperature of 600 °C, $Ti_3C_2T_x$-N/C-Ru-600 (TNCR-600), exhibited exceptional HER activity (η_{10} = 17 mV) and stability (160 h) under alkaline conditions. This work presented a simple and effective strategy for synthesizing composite catalysts, offering new insights into the design and regulation of high-performance Ru-based catalysts for hydrogen production.

Introducing nitrogen-doped carbon with highly-dispersed ruthenium (Ru) onto MXene through thermal decomposition of $RuCl_3$ coordinated with melamine and formaldehyde resin, the resulting catalyst, $Ti_3C_2T_x$-N/C-Ru-600 (TNCR-600), demonstrates excellent HER activity (η_{10} = 17 mV) and stability (160 h) under alkaline conditions, offering insights into the design of high-performance Ru-based catalyst.

Due to its high energy density and absence of carbon emissions during combustion, hydrogen (H_2) is recognized as an eco-friendly alternative energy source to conventional fossil fuels [1,2]. Since the beginning of this century, the development, storage, transportation, and application of H_2 have become the focal points within the energy domain, engendering transformative impacts on industrial production and human lifestyles [3]. Electrolytic water splitting stands as a pivotal approach to effectively acquiring clean and sustainable hydrogen energy [4]. To surmount the sluggish kinetics and high overpotential associated with the hydrogen evolution reaction (HER), proficient catalysts are imperative to facilitate the dissociation of H_2O or desorption of H_2. Presently, platinum (Pt) continues to be regarded as the benchmark electrocatalyst exhibiting superior HER activity [5]. Nonetheless, the scarcity of Pt-based catalysts and high commercial costs constitute a bottleneck impeding large-scale applications [6,7]. Hence, it is of utmost importance to explore alternative low-cost and resource-abundant electrocatalysts possessing high HER activity, thereby propelling the industrialization of water splitting.

Among the various candidates, Ru exhibits a Ru-H bond akin to the Pt-H bond (~65 kcal/mol). Furthermore, Ru is a member of the noble metal family related to Pt [8], with a cost of approximately 1/4 that of Pt [9]. Consequently, Ru has been proposed as a promising metal for the construction of HER electrocatalysts [10–13]. Nevertheless, the utilization of reducing agents or high-temperature pyrolysis is frequently necessary during the preparation process of Ru-based catalysts, which often results in the irreversible aggregation of Ru and significantly reduces its utilization efficiency, and undermines both the activity and stability of the resulting catalyst [14]. Therefore, it is crucial to contrive a simple and easy-operating method to load Ru onto a suitable substrate, which is important for preparing highly active and well-dispersed Ru-based catalysts [15]. So far, various conductive substrates have been combined with Ru to achieve efficient electrocatalytic hydrogen evolution. For exam-

* Corresponding authors.
E-mail addresses: yajunwang@wzu.edu.cn (Y. Wang), yitang@fudan.edu.cn (Y. Tang).

https://doi.org/10.1016/j.cclet.2023.109258
1001-8417/

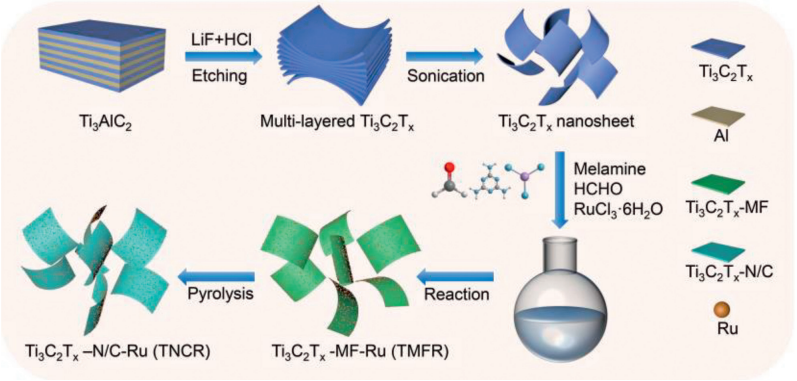

Fig. 1. Schematic illustration of the synthesis of $Ti_3C_2T_x$ MXene and TNCR.

ple, nanoporous carbon [16], graphene [17], MoS_2 [18], Mo_2C [19], carbon nanotubes [20], WO_x [21], MXene [22]. Among them, MXene materials possess large specific surface areas, abundant surface functional groups, high electronic conductivity, excellent surface activity, good hydrophilicity, and ease of handling, making them attractive for electrocatalytic hydrogen evolution [23–27].

As the alkaline HER involves two fundamental steps: water dissociation to produce adsorbed H and subsequent desorption of H_2 molecules [28], the utilization of a single active site to simultaneously execute these multi-step complex reactions often presents certain limitations. Ideally, an outstanding alkaline hydrogen evolution catalyst should simultaneously overcome the dissociation energy barrier of H_2O and have a low hydrogen adsorption energy to achieve overall high catalytic efficiency [29]. The coexistence of Ru NPs and Ru single-atom (Ru SA) is believed to synergistically catalyze the alkaline water electrolysis process for hydrogen production *via* accelerating water dissociation and H_2 desorption [30–32].

Herein, we report a facile approach to rationally controlling the Ru species on MXene surfaces for the optimization of HER performance. The $Ti_3C_2T_x$ MXene-based electrocatalyst with a highly dispersed Ru active phase (denoted as $Ti_3C_2T_x$-N/C-Ru, TNCR) was prepared by thermal cracking after the coordination of $RuCl_3$ with melamine and formaldehyde (MF) resin on the $Ti_3C_2T_x$ surface (Fig. 1). Importantly, the calcination temperature directly governed the size of Ru NPs and the proportion of Ru SA, thereby influencing the electronic valence distribution of Ru. Remarkably, the catalyst synthesized at a calcination temperature of 600 °C, denoted as TNCR-600, exhibited exceptional hydrogen evolution activity (η_{10} = 17 mV) and outstanding stability (160 h) under alkaline conditions. Toxicity experiments involving the treatment with either potassium thiocyanate (KSCN) or ethylenediaminetetraacetic acid (EDTA) further corroborated the prominence of Ru NPs as the primary active centers, working synergistically with Ru SA to achieve efficient electrocatalytic hydrogen evolution [31,33]. This study showcases a straightforward engineering strategy for composite material synthesis, offering novel insights into the effective design and fine-tuning of Ru-based efficient hydrogen evolution catalysts.

The TNCR was prepared through a facile two-step method (Fig. 1). Initially, Ru was anchored onto $Ti_3C_2T_x$ MXene *via* the chelation with the preloaded MF resin to form an intermediate product, TMFR, under a temperature of 80 °C in an oil bath. Subsequently, the Ru-anchored MF resin on $Ti_3C_2T_x$ MXene was thermally treated to result in N-doped carbon at different temperatures, yielding the target two-dimensional (2D) MXene-based electrocatalyst with a highly dispersed Ru phase (TNCR). The preparation of $Ti_3C_2T_x$ was a prerequisite for the synthesis of the TNCR. To synthesize ultrathin $Ti_3C_2T_x$ nanosheets, a mild etching and delamination method was employed on the Ti_3AlC_2 precursor. Scanning electron microscope (SEM) images showed that the unetched Ti_3AlC_2 exhibited large and thick block-like structures with closely-stacked layers (Fig. 2a). Elemental distribution mapping revealed an Al content of 6.08% (Fig. S1 in Supporting information). Following the LiF/HCl treatment and ultrasonication, the Al atomic layers were etched away from the Ti_3AlC_2, resulting in ultrathin $Ti_3C_2T_x$. Transmission electron microscope (TEM) images displayed transparent and highly dispersed $Ti_3C_2T_x$ nanosheets with a typical 2D layered topology (Fig. 2b). The lattice spacing corresponding to the $(01\bar{1}0)$ plane of MXene was measured as 0.265 nm, and the diffraction pattern exhibited hexagonal symmetry (Fig. S2 in Supporting information). Energy dispersive X-ray (EDX) spectroscopy elemental mapping analysis of the etched $Ti_3C_2T_x$ nanosheets showed uniform distribution of Ti and C elements without any signal of Al (Fig. S3 in Supporting information). The X-ray diffraction (XRD) spectrum of the MAX Ti_3AlC_2 powder matched well with the standard card JCPDS No. 52-0875, with the strongest diffraction peak at $2\theta \approx 39°$ corresponding to the (104) plane (Fig. S4 in Supporting information). After etching, the strong diffraction peak at 39.0° completely disappeared, and the (002) diffraction peak leftward shifted to 6.9° from 9.9° accompanied by an increased peak width [34], indicating the effective etching of the Al layers in MAX. These characterizations collectively demonstrate the successful preparation of ultrathin $Ti_3C_2T_x$.

The TNCR maintained the characteristic morphology of 2D flakes as observed of $Ti_3C_2T_x$ MXene (Fig. 2c and Fig. S5 in Supporting information), and no other impurity was found. Furthermore, high resolution transmission electron microscope (HRTEM) images provided evidence that the Ru NPs were evenly distributed on the $Ti_3C_2T_x$-N/C substrate (Figs. 2d-f). And the size of the Ru NPs exhibited a positive correlation with the temperature, indicating an increase in size as the temperature rises. Statistical analysis indicated that the average particle diameters of Ru NPs are 1.55, 1.96, and 3.14 nm in the TNCR-500, TNCR-600, and TNCR-700 samples obtained by calcination at 500, 600, and 700 °C, respectively. In addition to the Ru NPs, there were numerous isolated white dots presented in the high-angle annular dark field-scanning transmission electron microscopy (HAADF-STEM) images, suggesting the existence of Ru SA in TNCR (Figs. 2g and h). While Ru SA was presented in all TNCR samples calcined at the three different temperatures of 500–700 °C, the highest proportion of Ru SA was observed in TNCR-500, with the content significantly decreasing in TNCR-700 (Fig. S6 in Supporting information). This indicated that with increasing calcination temperature, Ru SA tended to aggregate and form Ru particles. EDX elemental mapping analysis confirmed the uniform distribution of Ru on the nanosheets (Fig. 2i, Figs. S7 and S8 in Supporting information).

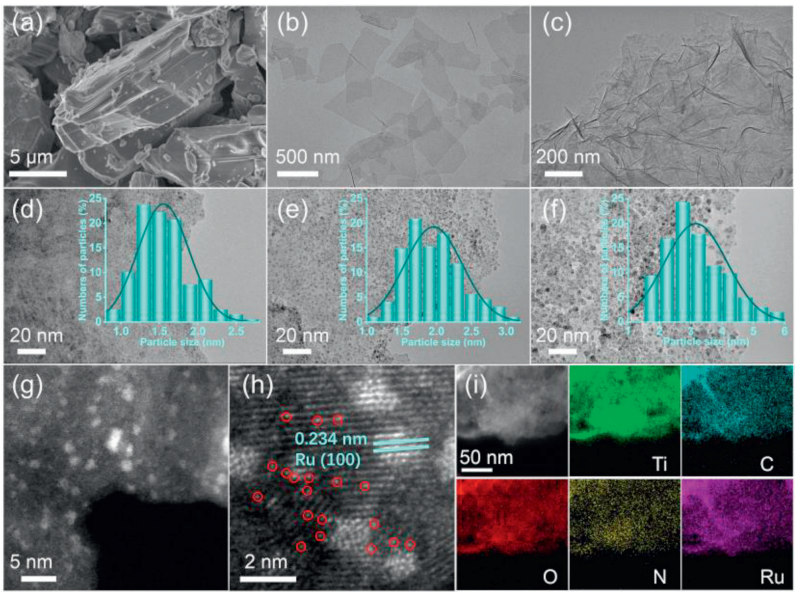

Fig. 2. Electron microscopy photographs of samples. (a) SEM image of Ti_3AlC_2. TEM images of (b) $Ti_3C_2T_x$, (c, e) TNCR-600, (d) TNCR-500, and (f) TNCR-700. The inset in (d, e, f) showed the statistical distribution of Ru particle sizes. (g, h) HAADF-STEM images and (i) EDX elemental mapping analysis of TNCR-600. The bright dots highlighted by the red circles in (h) were the Ru SA.

The MF resin played a crucial role in preserving the morphology of the 2D sheets and high dispersion of Ru species during the synthesis of TNCR. To compare, we synthesized a sample $Ti_3C_2T_x$-Ru (TR) without adding melamine and formaldehyde. In the absence of resin protection, the $Ti_3C_2T_x$ sheet experienced severe self-oxidation during the synthesis process, leading to the destruction of the 2D morphology and the formation of substantial amount of large TiO_2 particles in the TR sample (Fig. S9 in Supporting information). Meanwhile, owing to the absence of complexation with MF resins, the Ru species in TR samples presented a widen size distribution. Fig. S9c clearly displayed the lattice spacing of 0.352 nm corresponding to the (101) crystal plane of anatase TiO_2 [35,36], and 0.206 nm corresponding to the (101) crystal plane of Ru [37,38]. EDX elemental mapping analysis on TR samples disclosed that Ti and O regions significant overlapped each other while Ti and C exhibited less overlap, signifying substantial oxidation of the MXene material to generate TiO_2 (Fig. S10 in Supporting information). To further prove the importance of MF resins on the synthesis, a control sample (denoted as TNCR-600-c) was synthesized by the same process as TNCR-600, except no formaldehyde was added. As shown in Fig. S11 (Supporting information), the $Ti_3C_2T_x$ MXene substrate was also severely damaged, resulting in the formation of TiO_2 particles. In the EDX elemental mapping analysis, the Ti and O regions exhibited significant overlap as well (Fig. S12 in Supporting information). These results illustrated the necessity of MF on the preparation of 2D composite catalyst of highly dispersed-Ru on N-doped Carbon/MXene nanosheets.

XRD analysis can elucidate alterations in the phase structure and composition of materials. Different from that of TR sample (Fig. S13 in Supporting information) and TNCR-600-c (Fig. S14 in Supporting information) where displayed the pattern of well crystallized anatase TiO_2 (JCPDS No. 21-1272), the XRD patterns of TNCR samples exhibited subtle anatase TiO_2 peaks at around 25.3° (Fig. 3a), and a faint peak of rutile TiO_2 (JCPDS No. 21-1276) emerged near 27.4° in that of TNCR-700. These results clearly proved the protective role of MF resin in the formation of TNCR electrocatalysts. Additionally, TNCR-500, TNCR-600, and TNCR-700 displayed a weakening and broadening of the XRD diffraction peak

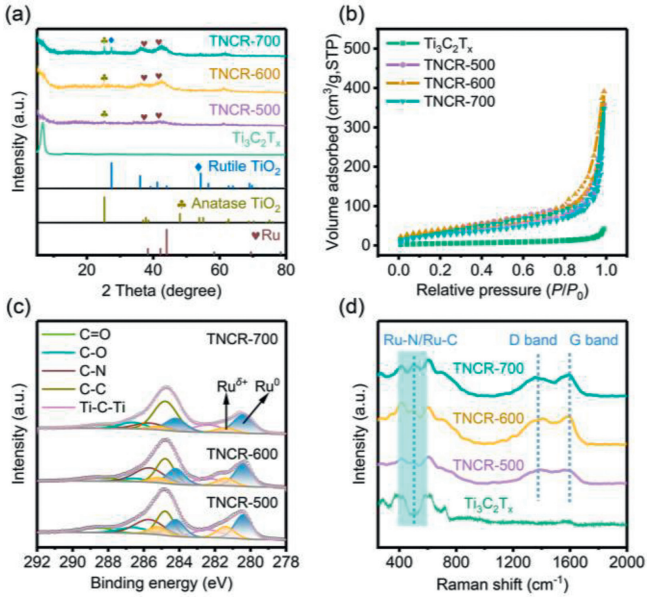

Fig. 3. Characterization of TNCR samples. (a) XRD patterns, (b) N_2 adsorption-desorption isotherms, (c) XPS patterns, and (d) Raman spectroscopy of TNCR samples.

in the range of 38°−45° (JCPDS No. 65-1863) corresponding to the highly dispersed Ru nanocrystals. Concurrently, the strongest peak at 6.9° of the (002) crystal plane of $Ti_3C_2T_x$ shifted to the left in the XRD pattern of TNCRs, signifying that the introduction of N/C and Ru disturbed and expanded the interlayer spacing of $Ti_3C_2T_x$ in the *c*-axis direction. This further confirmed that the synthesis method of composite materials effectively mitigated the stacking of $Ti_3C_2T_x$ nanosheets. N_2-sorption experiments revealed that the specific surface area of $Ti_3C_2T_x$ was 16.4 m^2/g, while those of TNCR-500, TNCR-600, and TNCR-700 were measured as 117.4, 132.4 and 96.1 m^2/g, respectively (Fig. 3b). The large hysteresis loop at high relative pressure indicated that TNCR samples exhibited large

meso/macroporosity arising from the introduction of Ru species and N/C contributions, which would facilitate the electrolyte infiltration and enhance the exposure of active sites, consequently improving the HER performance.

The valence state of Ru in the TNCR material significantly impacted its HER performance. XPS analysis revealed that the binding energy of the Ru 3d orbital overlaps with that of the C 1s orbital. Fortunately, the binding energies of C 1s and Ru $3d_{5/2}$ do not completely overlap, allowing Ru $3d_{5/2}$ to be uniquely identified and differentiated [39]. The XPS spectrum of Ru $3d_{5/2}$ in the TNCR exhibited two distinct peaks: Ru^0 $3d_{5/2}$ and $Ru^{\delta+}$ $3d_{5/2}$, confirming that the valence state of Ru primarily included both zero-valent Ru^0 ($Ru^0{}_{5/2}$: 280.4 eV) from Ru NPs and positive $Ru^{\delta+}$ ($Ru^{\delta+}{}_{5/2}$: 281.4 eV) from the coexisting Ru SA (Fig. 3c) [30], which coincided with the TEM results from Fig. 2h and Fig. S6. The $Ru^{\delta+}/(Ru^{\delta+}+Ru^0)$ ratios were determined to be 32.74%, 24.84%, and 19.14% for TNCR-500, TNCR-600, and TNCR-700, respectively, signifying an increased tendency of Ru SA to aggregate into Ru NPs as the annealing temperature rises. Furthermore, the N 1s spectrum was subjected to peak deconvolution, revealing five distinct peaks corresponding to Ti-N (396.3 eV), pyridinic N (397.9 eV), Ru-N (399.3 eV), pyrrolic N (400.2 eV), and graphitic N (401.6 eV) (Fig. S15 in the Supporting information). With the annealing temperature increasing, there is an increase in the content of Ti-N and graphitic N, while the content of pyridinic N, Ru-N, and pyrrolic N decreases. This observation suggests that higher temperatures lead to a greater degree of graphitization of nitrogen, concomitant with a decrease in the content of the Ru SA, corresponding to Ru-N. The Raman characteristic peaks of $Ti_3C_2T_x$ MXene correspond to the in-plane shear modes (E_g) of Ti, C, and surface functional group atoms at positions of 286 (ω5), 395 (ω5), and 625 cm^{-1} (ω4), respectively. A_{1g} symmetric vibrations of Ti and C atoms occur at 201 (ω2) and 716 cm^{-1} (ω3), as shown in Fig. S16 (Supporting information) [40]. In the TNCR series samples, the peaks within the 400–600 cm^{-1} range exhibit distinct differences from those in $Ti_3C_2T_x$, featuring an additional peak near 503 cm^{-1}. This peak is absent in the Raman spectrum of $Ti_3C_2T_x$ and could be assigned to the stretching vibrations of Ru-N/Ru-C bonds [41]. Furthermore, the presence of distinct D and G bands at wavenumbers 1380 and 1557 cm^{-1} were attributed to the carbonaceous matrix formed during the reaction process. The calculated I_D/I_G ratios were found to be 1.0, 0.95, and 0.94 for TNCR-500, TNCR-600, and TNCR-700, respectively, suggesting a progressive increase in the relative intensity of the I_G band and enhanced carbon graphitization as the temperature rises [42]. The I_D/I_G ratio can also be indicative of the defect content in graphite carbon, with a higher I_D/I_G ratio indicating a greater number of defects. The highest defect density in TNCR-500 is likely caused by the lowest annealing temperature in this sample preparation. This agrees well with the literature report that the elevated temperature favors the crystallization of graphitic carbon, leading to a reduction in defect density [43–45].

The HER performances of TNCR as well as carbon paper (CP), $Ti_3C_2T_x$, TNC ($Ti_3C_2T_x$-NC), commercial Ru/C, and Pt/C were investigated in 1.0 mol/L KOH using a three-electrode system (Fig. 4a). The comparative evaluation of various samples revealed that CP, $Ti_3C_2T_x$, and TNC displayed negligible HER activity. Fig. 4b depicted the overpotential at 10 mA/cm^2 and 100 mA/cm^2 (η_{10} and η_{100}) of TNCR samples as well as those of commercial Ru/C and Pt/C. TNCR-600 exhibited the highest catalytic activity, necessitating a significantly lower overpotential of 17 mV to achieve a current density of 10 mA/cm^2. In contrast, TNCR-500 required an overpotential of 50 mV at 10 mA/cm^2, TNCR-700 required 36 mV, commercial Ru/C needed 42 mV, and commercial Pt/C necessitated 24 mV. The corresponding overpotential of each sample at η_{100} had the same trend, and the overpotential of TNCR-600 was only 62 mV. These results indicated that TNCR-600 indeed possessed satisfactory basic HER performance and was comparable to or even better than some recently reported Ru-based electrocatalysts (Fig. 4e and Table S1 in Supporting information).

Mass activity was a crucial parameter for evaluating the HER performance, defined as the current normalized to the mass loading of the catalyst [46]. According to the inductively coupled plasma atomic emission spectroscopy (ICP-AES) results, the Ru contents in TNCR-500, TNCR-600, TNCR-700 were measured as 7.38, 7.52, and 8.32 wt%, respectively. The calculated mass activities at 100 mV for TNCR-500, TNCR-600, TNCR-700 were 0.56, 2.84 and 0.95 A/mg_{Ru}, respectively. The mass activity of TNCR-600 demonstrated exceptional performance, even at 3.4 times that of commercial Ru/C (0.84 A/mg_{Ru}) and 3.1 times that of commercial Pt/C (0.93 A/mg_{Pt}). Assuming that all the Ru atoms in the catalyst are active sites participating in the HER, the calculated TOF values for TNCR-500, TNCR-600, TNCR-700, Ru/C, and Pt/C at 100 mV overpotential are 0.29, 1.49, 0.50, 0.44, and 0.49 s^{-1}, respectively. For TNCR-600 exhibiting the highest TOF value, we also calculated TOF values for the sample at overpotentials of 10, 20, 30, 70, and 150 mV, resulting in values of 0.02, 0.1, 0.21, 0.86, and 2.47 s^{-1}, respectively. As summarized in Table S1, the TOF values for the TNCR-600 sample are at a favorable level when compared to the literature-reported TOF values calculated by the same method, in which all Ru atoms in the sample were assumed to participate in the reaction.

The Tafel slope was further calculated to reveal the HER kinetics. In general, the Tafel slope correlated with the polarization curve, where a smaller Tafel slope indicated a faster hydrogen generation rate achieved by applying an overpotential. The Tafel slope was indicative of the material's kinetic behavior during the electrode reaction process [47]. The alkaline HER encompassed two pivotal processes: (1) The adsorption and dissociation of H_2O on the catalyst's surface (Volmer step: $H_2O + * + e^- \rightarrow H^* + OH^-$); and (2) the desorption of hydrogen (H^*) (Tafel step: $2H^* \rightarrow H_2$; Heyrovsky step: $H_2O + H^* + e^- \rightarrow H_2 + OH^-$) [48,49]. Specifically, the Tafel slope of TNCR-600 was 28.3 mV/dec, which was lower than that of TNCR-500 (69.2 mV/dec), TNCR-700 (49.8 mV/dec), commercial Ru/C (60.3 mV/dec) and commercial Pt/C (31.6 mV/dec) (Fig. 4c). These results suggested TNCR-600 and commercial Pt/C follow the Volmer-Tafel step, whereas TNCR-500, TNCR-700, and commercial Ru/C conformed to the Volmer-Heyrovsky step [50,51]. The rate-determining step for these samples involved the desorption of the hydrogen intermediate H^*, leading to the formation of H_2. In the case of TNCR-600, the optimized electronic structure of Ru enabled a more favorable balance between the dissociation of H_2O and H_2 desorption, thereby facilitating the kinetics of HER. These results indicated that the overall performance of TNCR-600 was superior to that of the commercial Ru/C and Pt/C catalysts.

The electrochemically active surface area (ECSA) of the samples was evaluated by the double layer capacitance (C_{dl}), which was tested using a typical cyclic voltammetry (CV) method (Fig. S17 in Supporting information). As shown in Fig. 4d, the C_{dl} value of TNCR-600 was 38.9 mF/cm^2, significantly larger than the 6.75 mF/cm^2 of TNCR-500 and the 14.9 mF/cm^2 of TNCR-700. A higher C_{dl} meant a larger active surface area of the electrocatalyst, which could increase the contact of the electrolyte with the exposed active sites of the catalyst, thereafter enhancing the electrocatalytic activity [52]. In addition, electrochemical impedance spectroscopy (EIS) was also performed to study the electrode kinetics of the samples (Fig. S18 in Supporting information). The charge transfer resistance (R_{ct}) values for TNCR-600, TNCR-700, the reference commercial Ru/C and Pt/C were measured to be 1.6, 1.8, 1.5 and 1.7 Ω, respectively. The observed differences in R_{ct} values among these samples were relatively small. However, TNCR-500, due to its lower calcination temperature, exhibited a lower carbonization degree compared to the other samples, resulting in a higher R_{ct} value of 4.8 Ω.

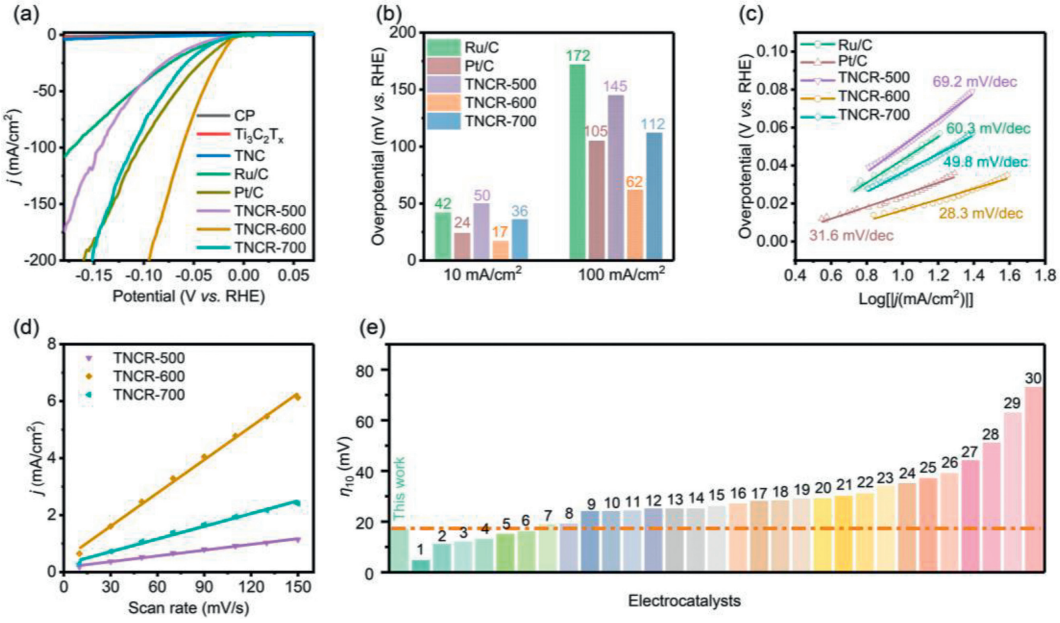

Fig. 4. Alkaline HER performance test of various samples. (a) HER polarization curves. (b) The corresponding overpotentials of different samples at 10 mA/cm^2 and 100 mA/cm^2. (c) Tafel plots for the corresponding materials. (d) Calculated double-layer capacitance (C_{dl}) was used to estimate the electrochemically active surface area of the different samples. (e) Comparison of η_{10} values for TNCR-600 and other recently reported Ru-based HER electrocatalysts in alkaline media (Information for the referenced samples was summarized in Table S1).

These results revealed that TNCR-600 displayed the highest HER activity among the tested samples. This was primarily attributed to the enhanced conductivity achieved through the optimal calcined temperature of TNCR-600. As reported in the leading results of recent literatures on Ru-based electrocatalysts for alkaline hydrogen evolution, the coexistence of Ru NPs and Ru SA could improve the hydride coupling and water dissociation kinetics, thus synergistically enhancing alkaline hydrogen evolution performance [30,31,42,46,49,53] although the viewpoint for the role of each component remained controversial [41]. The well-balanced distribution ratio of Ru SA and Ru NPs in TNCR-600 might contribute to its highest HER activity among the tested samples.

The HER performance of TNCR-600 was also evaluated in acidic (0.5 mol/L H_2SO_4) and neutral (1 mol/L PBS) solutions. The LSV test results (Fig. 5a) revealed that TNCR-600 exhibits overpotentials (η_{10}) of 49 and 63 mV in acidic and neutral environments, respectively. As shown in Fig. 5b, the corresponding Tafel slopes were measured to be 53.1 and 97.1 mV/dec. Furthermore, the EIS measurements for TNCR-600 yielded values of 7.6 Ω in H_2SO_4 and 8.1 Ω in PBS, as illustrated in Fig. 5c. The C_{dl} values were determined to be 34.5 and 31.4 mF/cm^2 under acidic and neutral conditions, respectively (Fig. 5d and Fig. S19 in Supporting information). These comprehensive tests collectively confirmed the excellent HER activity of TNCR-600 across the entire pH range.

To gain deeper insights into the roles of ultrafine Ru NPs and Ru SA in TNCR-600, relevant poisoning experiments were conducted to probe the impact of each active site. EDTA and KSCN were used as ligands for the poisoning experiments, enabling a direct comparison of the contributions of Ru NPs and Ru SA in TNCR-600. Given that EDTA primarily coordinates with Ru SA, while KSCN could interact with both Ru NPs and Ru SA, EDTA inhibited the activity of a single Ru SA, while KSCN leaded to the deactivation of all Ru species [33,42,54]. As shown in Fig. 6a, TNCR-600 exhibited partial deactivation under EDTA induction, with an increase in overpotential (η_{10}) from 17 mV to 23 mV. However, the introduction of KSCN significantly deteriorated the HER performance of TNCR-600 with η_{10} overpotential increasing to 137 mV, indicating the

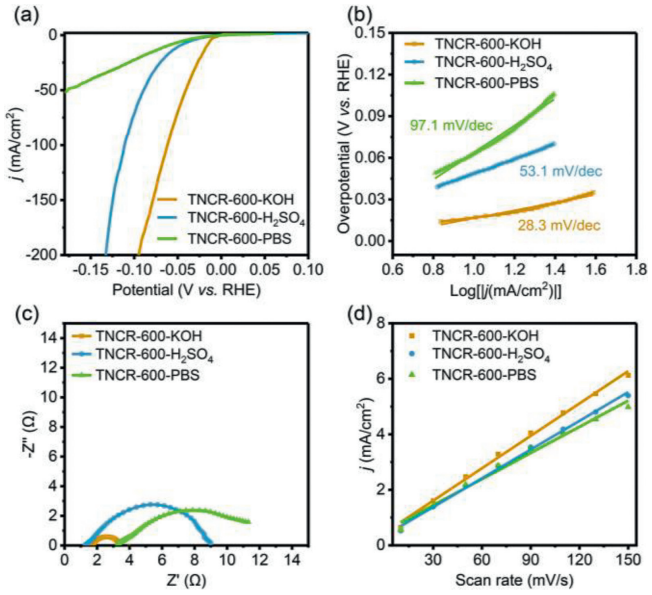

Fig. 5. HER performance testing across the entire pH range. (a) HER polarization curves, (b) Tafel plots, (c) impedance, and (d) calculated double-layer capacitance of TNCR-600 at different pH values.

near-complete deactivation of Ru species. The substantial disparity in electrocatalytic performance observed between EDTA and KSCN-poisoned TNCR-600 underscores the dominance of Ru nanoparticles as the primary active sites for HER, as opposed to the Ru single atoms.

Long-term electrocatalytic stability was a crucial parameter for assessing the performance of electrocatalysts. As illustrated in Fig. 6b, the HER activity of TNCR-600 remained stable even after undergoing 20,000 cycles of CV testing. To simulate real-world industrial applications, we further evaluated the durability of the electrocatalyst under a high current density of 400 mA/cm^2 in

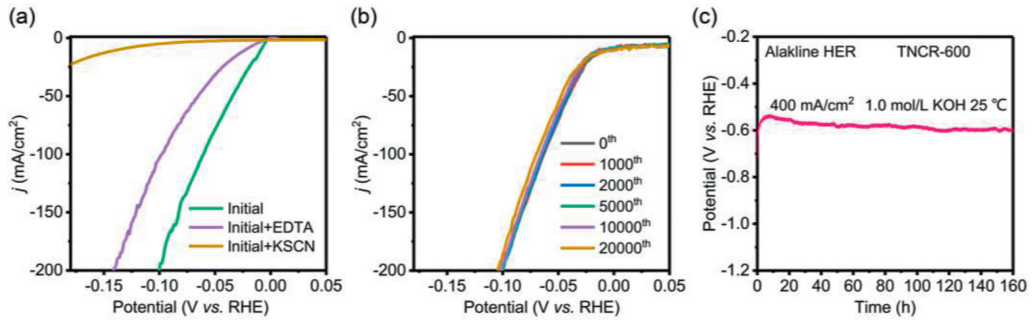

Fig. 6. Toxicity test and stability of TNCR-600. (a) The HER polarization curves of TNCR-600 poisoned by EDTA (10 mmol/L) and KSCN (10 mmol/L), respectively. (b) Durability measurements for TNCR-600 at the initial, 1000th, 2000th, 5000th, 10000th, and 20000th cycles. (c) Chronopotentiometric (CP) curve recorded at a constant current density of 400 mA/cm^2 (without *iR* correction).

1 mol/L KOH. TNCR-600 demonstrated remarkable stability, maintaining a consistent potential over a 160-h period during the alkaline HER process (Fig. 6c). Furthermore, TNCR-600 showed stability for over 120 h in 0.5 mol/L H_2SO_4 and in 1.0 mol/L PBS (Fig. S20 in Supporting information). These results affirmed the robust and reliable performance of TNCR-600 as a promising HER catalyst.

To comprehensively grasp the catalytic implications of active sites and establish a unified framework, we conducted density functional theory (DFT) calculations to explore the respective energies associated with Ru_{SA}+Ru_{NP}-N/C-MXene, Ru_{SA}-N/C-MXene, Ru_{NP}-N/C-MXene, and Ru_{SA}+Ru_{NP}-N/C. The outcomes of these calculations, concerning hydrogen (*H) binding energy and hydrogen adsorption free energy (ΔG_{H^*}), are presented in Figs. S21 and S22 (Supporting information). From the depicted data, it is evident that Ru_{SA}+Ru_{NP}-N/C-MXene exhibits the most favorable H* binding energy and the lowest ΔG_{H^*}, indicative of a synergistic effect between the Ru_{SA} and Ru_{NP} in diminishing ΔG_{H^*}. Additionally, we computed the corresponding energies for the Ru_{SA}+Ru_{NP}-N/C sample in the absence of MXene. The results revealed that in the absence of MXene, Ru_{SA}+Ru_{NP}-N/C has the highest H* binding energy and ΔG_{H^*}, thereby impeding hydrogen desorption and negatively impacting HER activity. This underscores the role of the MXene in facilitating electron transfer within the TNCR electrocatalysts, thereby reducing ΔG_{H^*} and enhancing the electrocatalytic hydrogen evolution activity.

In summary, this work employed a facile and practical method to load highly dispersed Ru with rationally controllable species on N-doped C-modified $Ti_3C_2T_x$ surface through a coordination reaction between the MF resin and $RuCl_3$, followed by thermal decomposition. $Ti_3C_2T_x$ provided a large specific surface area and good conductivity. The strategy of using MF resin effectively prevented Ru aggregation to maintain the monodisperse distribution of ultrasmall Ru nanoparticles, and effectively prevented the oxidation of $Ti_3C_2T_x$. By tuning the calcination temperature, the size of Ru NPs and the appropriate proportion of Ru SA can be controlled, thereby readily tailoring the HER performance. The sample annealed at 600 °C (TNCR-600) exhibited exceptional HER activity (η_{10} = 17 mV) and stability (160 h) under alkaline conditions. The poisoning experiments confirmed that Ru NPs served as the primary active centers. This study demonstrates a facile strategy for synthesizing composite materials, providing new insights into the design and modulation of efficient Ru-based HER catalysts for advancing the industrialization and sustainable development of hydrogen energy.

Declaration of competing interest

The authors hereby declare that they have no competing financial interests or personal relationships that might have influenced the work and findings presented in this paper.

Acknowledgments

This work was financially supported by the National Key R&D Program of China (No. 2018YFA0209402) and the National Natural Science Foundation of China (Nos. 22088101, 22175132, 22072028).

Supplementary materials

Supplementary material associated with this article can be found, in the online version, at doi:10.1016/j.cclet.2023.109258.

References

[1] F. Dawood, M. Anda, G.M. Shafiullah, Int. J. Hydrogen Energy 45 (2020) 3847–3869.
[2] Z.S. Li, Y. Yue, J.C. Peng, et al., Chin. Chem. Lett. 34 (2023) 107119.
[3] A. Kovač, M. Paranos, D. Marciuš, Int. J. Hydrogen Energy 46 (2021) 10016–10035.
[4] L. Cai, J.T. Huo, P. Zou, et al., ACS Appl. Mater. Interfaces 14 (2022) 15243–15249.
[5] J. Park, S. Lee, H.E. Kim, et al., Angew. Chem., Int. Ed. 58 (2019) 16038–16042.
[6] R.R. Song, J.H. Han, M. Okugawa, et al., Nat. Commun. 13 (2022) 5157.
[7] L.Y. Xiu, W. Pei, S. Zhou, et al., Adv. Funct. Mater. 30 (2020) 1910028.
[8] J. Yu, Q.J. He, G.M. Yang, et al., ACS Catal. 9 (2019) 9973–10011.
[9] B. Tang, X.D. Yang, Z.H. Kang, et al., Appl. Catal. B 278 (2020) 119281.
[10] W.J. Luo, Y.J. Wang, C.W. Cheng, Mater. Today Phys. 15 (2020) 100274.
[11] Y.J. Yang, Y.H. Yu, J. Li, et al., Nanomicro Lett. 13 (2021) 160.
[12] N. Wang, D.D. Ma, S.H. Zhou, et al., Chin. Chem. Lett. 34 (2023) 107788.
[13] Y.L. Wu, N. Xie, X.F. Li, et al., Chin. J. Struct. Chem. 40 (2021) 1346–1356.
[14] Q.R. Liang, Q.Z. Li, L. Xie, et al., ACS Nano 16 (2022) 7993–8004.
[15] H.X. Yao, X.K. Wang, K. Li, et al., Appl. Catal. B 312 (2022) 121378.
[16] Y.L. Wu, X.F. Li, Y.S. Wei, et al., Adv. Mater. 33 (2021) 2006965.
[17] Y. Ding, K.W. Cao, J.W. He, et al., Chin. J. Catal. 43 (2022) 1535–1543.
[18] J. Wang, W.H. Fang, Y. Hu, et al., Appl. Catal. B 298 (2021) 120490.
[19] K.X. Wang, S. Wang, K.S. Hui, et al., Carbon Energy 4 (2022) 856–866.
[20] X.L. Xiong, W. Geng, M.N. Cao, et al., Chin. Chem. Lett. 34 (2023) 107717.
[21] L.X. Peng, L. Su, X. Yu, et al., Appl. Catal. B 308 (2022) 121229.
[22] Y.Y. Yang, Z.L. Yu, X.W. An, et al., Int. J. Hydrogen Energy 48 (2023) 9163–9171.
[23] Y.C. Wu, W. Wei, R.H. Yu, et al., Adv. Funct. Mater. 32 (2022) 2110910.
[24] X. Wang, J. Ding, W.Q. Song, et al., Adv. Energy Mater. 13 (2023) 2300148.
[25] C.X. Wang, X.X. Wang, T.Y. Zhang, et al., J. Mater. Chem. A 10 (2022) 18195–18205.
[26] A.Q. Kong, M. Peng, H.Z. Gu, et al., Chem. Eng. J. 426 (2021) 131234.
[27] M. Bat-Erdene, M. Batmunkh, B. Sainbileg, et al., Small 17 (2021) 2102218.
[28] J.S. Wang, S.S. Xin, Y. Xiao, et al., Angew. Chem. Int. Ed. 61 (2022) 202202518.
[29] X.M. Wang, G.F. Long, B. Liu, et al., Angew. Chem. Int. Ed. 62 (2023) 202301562.
[30] S.R. Wang, M.M. Wang, Z. Liu, et al., ACS Appl. Mater. Interfaces 14 (2022) 15250–15258.
[31] Q. He, Y.Z. Zhou, H.W. Shou, et al., Adv. Mater. 34 (2022) 2110604.
[32] T.M. Luo, J.F. Huang, Y.Z. Hu, et al., Adv. Funct. Mater. 33 (2023) 2213058.
[33] P.P. Su, W. Pei, X.W. Wang, et al., Angew. Chem., Int. Ed. 60 (2021) 16044–16050.
[34] G.N. Cai, Z.Z. Yu, P. Tong, et al., Nanoscale 11 (2019) 15659–15667.
[35] T. Wu, J.C. Fan, Q.X. Li, et al., Adv. Energy Mater. 8 (2018) 1701799.
[36] T.F. Lou, S.Z. Song, X.H. Gao, et al., J. Colloid Interface Sci. 617 (2022) 663–672.
[37] L.G. Chen, Y.P. Li, X. Liang, Adv. Funct. Mater. 31 (2021) 2007344.
[38] P. Zhu, Y.L. Shen, L.X. Dai, et al., ACS Appl. Mater. Interfaces 14 (2022) 1452–1459.
[39] W.J. Dong, Y.J. Zhang, J. Xu, et al., Cell Rep. Phys. Sci. 1 (2020) 100026.
[40] L. Xiu, Z. Wang, M. Yu, et al., ACS Nano 12 (2018) 8017–8028.
[41] B. Lu, L. Guo, F. Wu, et al., Nat. Commun. 10 (2019) 631.

[42] X.L. Fan, C. Liu, M.Y. Wu, et al., Appl. Catal. B 318 (2022) 121867.
[43] J.Esohe Omoriyekomwan, A. Tahmasebi, J. Zhang, et al., Nanomaterials 12 (2022) 737.
[44] J. Lara-Romero, J.C. Calva-Yañez, J. Lopez-Tinoco, et al., Fullerenes Nanotubes Carbon Nanostruct. 19 (2011) 483–496.
[45] E.G. Ertane, A. Dorner-Reisel, O. Baran, et al., Adv. Tribol. 2018 (2018) 176318.
[46] Q. Hu, G. Li, X. Huang, et al., J. Mater. Chem. A 7 (2019) 19531–19538.
[47] W.H. Huang, X.M. Li, D.Y. Yu, et al., Nanoscale 12 (2020) 19804–19813.
[48] H.J.W. Li, K. Liu, J.W. Fu, et al., Nano Energy 82 (2021) 105767.
[49] J. Peng, Y.H. Chen, K. Wang, et al., Int. J. Hydrogen Energy 45 (2020) 18840–18849.
[50] Y.K. Tian, A.J. Huang, Z.G. Wang, et al., Chem. Eng. J. 426 (2021) 131827.
[51] M. Xu, L. Han, Y.J. Han, et al., J. Mater. Chem. A 3 (2015) 21471–21477.
[52] X.Z. Sun, X.Y. Gao, J. Chen, et al., ACS Appl. Mater. Interfaces 12 (2020) 48591–48597.
[53] C. Hu, E.H. Song, M.Y. Wang, et al., Adv. Sci. 8 (2021) 2001881.
[54] D. Cao, J.Y. Wang, H.X. Xu, et al., Small 17 (2021) 2101163.